

Robust Control of a Fluxonium Qubit

Thomas Propson,^{1,2,*} Brian Jackson,³ Zac Manchester,³ and David I. Schuster^{1,2,4}

¹*James Franck Institute, University of Chicago, Chicago, Illinois 60637, USA*

²*Department of Physics, University of Chicago, Chicago, Illinois 60637, USA*

³*Department of Aeronautics and Astronautics Engineering,
Stanford University, 496 Lomita Mall, Stanford, CA 94305*

⁴*Pritzker School of Molecular Engineering, University of Chicago, Chicago, Illinois 60637, USA*

(Dated: November 6, 2020)

The ability to engineer high fidelity gates on quantum processors in the presence of systematic errors and decoherence remains the primary challenge requisite to achieving quantum advantage. Quantum optimal control (QOC) techniques have proven effective in experimentally realizing high fidelity gates, but they require exquisite calibration to be performant. We apply robust trajectory optimization techniques to suppress gate errors arising from system parameter deviations and noise. We propose a method that takes advantage of deviant parameter derivative information while maintaining computational efficiency by utilizing mixed-mode differentiation. Additionally, completely modeling decoherence effects due to longitudinal relaxation requires integrating the Lindblad master equation, which is computationally expensive. We propose a computationally efficient metric and utilize time-optimal control to achieve high fidelity gates in the presence of longitudinal relaxation. We demonstrate these techniques numerically on a fluxonium qubit with realistic experimental parameters and constraints, achieving orders of magnitude gate error reductions from our baseline gate set.

I. INTRODUCTION

Quantum optimal control (QOC) techniques are a class of optimization algorithms for accurately and efficiently manipulating quantum systems. Early techniques were proposed for nuclear magnetic resonance experiments [1], and applications now include superconducting circuits [2–6], neutral and ionized atoms [7], nitrogen-vacancy centers in diamond [8], and Bose-Einstein condensates [9]. For quantum computation QOC techniques are employed to achieve high fidelity gates while adhering to experimental constraints. The decision variables of the optimization problem are the time-dependent control parameters, particular to the quantum system, that govern its evolution. Experimental errors may cause the system evolution to deviate from that predicted in optimization, hampering performance. The field of classical control theory has developed robust control techniques to encode experimental errors in optimization objectives, improving experimental performance (citations appreciated). In this work we employ robust control techniques to mitigate realistic system parameter deviations and decoherence that arise when controlling a superconducting fluxonium qubit.

Analytic and numerical techniques for QOC have been remarkably successful in designing high fidelity gates (citations needed). In addition to the high simulated fidelities which can be obtained with these techniques, it is desirable for the resultant quantum state trajectory to be insensitive to experimental errors such as parameter drift, noise, and finite control resolution. Quantum state

trajectories that are insensitive to these effects are said to be robust. In line with this objective, recent work has sought to mitigate decoherence and errors due to parameter deviations. Considering the dynamical and geometric phases of quantum state trajectories has led to analytic methods for mitigating errors due to parameter deviations and pure dephasing [6, 10–12]. Floquet techniques have been experimentally demonstrated to simultaneously mitigate decoherence due to longitudinal relaxation and pure dephasing [3, 13]. Numerical QOC techniques have been adapted to mitigate longitudinal relaxation by modeling master equations [8] and employing Monte Carlo style quantum trajectories [14]. Additionally, efforts have been made to incorporate experimental feedback into optimization [3]. Comprehensive tools that interleave characterization and pulse design are under active development [15].

In this work we develop robust trajectory optimization techniques to mitigate errors arising from longitudinal relaxation, parameter deviations, and $1/f$ flux noise on the fluxonium qubit presented in [12]. We perform these optimization using the ALTRO method [16] which combines the iterative, indirect shooting flavor of methods such as GOAT [17], GRAPE [1, 5], and Krotov’s [18] with the augmented Lagrangian method. The augmented Lagrangian method allows us to enforce arbitrary, simultaneous constraints and achieve fast convergence without being restricted to the constraint manifold. To mitigate errors due to longitudinal relaxation, we perform time-optimal control and encode the dependence of longitudinal relaxation on the controls in an efficient optimization objective that does not pay the increased computational cost of integrating a master equation. Additionally, we consider three robust trajectory optimization techniques to make the quantum state trajectory ro-

* tcropson@uchicago.edu

bust to parameter deviations. The first is the sampling method, which has been applied previously in the context of QOC [8, 19, 20]. The second is the unscented sampling method, which derives from the unscented transformation used for non-linear Kalman filtering [21–23]. We propose a third method, which uses derivative information of parameter deviations with respect to the quantum state trajectory. We make this method efficient by employing mixed-mode differentiation.

This paper is outlined as follows. First, we introduce the ALTRO method in the context of QOC. We describe realistic constraints for the fluxonium and map them to the ALTRO method. Then, we outline a method for making the optimization aware of longitudinal relaxation. Next, we outline three methods for achieving robustness to static parameter deviations. Finally, we employ the robust control techniques to mitigate $1/f$ flux noise.

II. QOC + AL-ILQR

(QOC Problem Statement) Here we introduce the notation we will use throughout the paper, review the quantum optimal control problem statement, and introduce the trajectory optimization framework. Quantum optimal control concerns the evolution of a quantum state $|\psi(t)\rangle$ governed by the time-dependent Schroedinger equation (TDSE)

$$i\hbar \frac{d}{dt} |\psi\rangle = H(u(t), t) |\psi\rangle \quad (1)$$

The evolution is sometimes cast with the evolution of a density matrix under the Lindblad master equation to model the decoherence of the state explicitly. The Hamiltonian has an arbitrary dependence on the possibly multi-valued controls $u(t)$. The controls are so called because they are the means the experimentalist has to act on the system. Numerical quantum optimal control techniques make the problem tractable by discretizing the problem into N knot points (time steps). Typical explicit integration techniques for the TDSE include exponential integrators and integrators of the Runge-Kutta type

Quantum optimal control seeks the control parameters that minimize a functional $J(u(t))$. In the simplest case the functional is $J = 1 - |\langle \psi_f | \psi_N(u(t)) \rangle|^2$ the infidelity between the initial state evolved to the final knot point ($|\psi_N(u(t))\rangle$) and the target state ($|\psi_f\rangle$). In general J is a linear combination of cost functions on the state, e.g. forbidden-state occupation, as well as cost functions on the controls, e.g. the norm of the control amplitudes [5]. Typical quantum optimal control algorithms employ automatic differentiation to compute first order information for the functional ($\nabla_u J(u)$). They employ a first-order optimizer to minimize J with respect to u .

(AL-iLQR Problem Statement) The trajectory optimization literature solves a more general class of non-

linear programs that resemble the quantum optimal control problem. The quantum optimal control problem is a specific case of the linear quadratic regulator (LQR). LQR is so called because the dynamics are linear in the state and the functional is quadratic in the state. In the LQR formulation the same functional is evaluated at each knot point

$$J_{\text{iLQR}} = \tilde{x}_N^T Q_N \tilde{x}_N + \sum_{k=0}^{N-1} \tilde{x}_k^T Q_k \tilde{x}_k + u_k^T R_k u_k \quad (2)$$

where $\tilde{x}_k = x_k - x_f$ is the difference between the state at knot point k and final state, u_k are the controls, and Q_k, R_k are matrices that define the penalty metric. The state is propagated using a dynamics function $x_{k+1} = f(x_k, u_k, t_k, \Delta t_k)$. In the case of quantum optimal control $|\psi_k\rangle \subseteq x_k$ and f encodes the TDSE dynamics. In the following we refer to $|\psi\rangle$ as the state, x as the augmented state, and u as the augmented controls.

The advantage of the LQR formulation is that there exists a dynamic programming algorithm to compute the optimal update to the augmented controls (u_k) which minimizes the functional ($J_{\text{iLQR},k}$) for each knot point. This algorithm proceeds by deriving a recurrence relation between knot points k and $k+1$ for the optimal feedback law—known as the Ricatti recursion (see Appendix). The iterative LQR (iLQR) algorithm computes J_{iLQR} and applies the Ricatti recursion to all knot points on multiple executions.

In order to incorporate constraints we employ the augmented Lagrangian method. Constraints are contributions to the functional of arbitrary form $c_k(x_k, u_k)$ which are zero or negative when the constraint is satisfied. The AL-iLQR method associates a penalty multiplier with the functional that estimates the constraint's Lagrange multiplier. The algorithm updates the penalty multiplier between iLQR executions. In this scheme the functional takes the form

$$J_{\text{AL-iLQR}} = (\lambda_k + \frac{1}{2} I_{\mu_k} c_k(x_k, u_k))^T c_k(x_k, u_k) + J_{\text{iLQR}} \quad (3)$$

where λ_k is a Lagrange multiplier and I_{μ_k} is a penalty matrix with μ_k along the diagonal. λ_k and μ_k are updated after each augmented Lagrangian iteration according to

$$\lambda_{k_i} \leftarrow \max(0, \lambda_{k_i} + \mu_{k_i} c_{k_i}(x_k^*, u_k^*)) \quad (4)$$

$$\mu_{k_i} \leftarrow \phi \mu_{k_i} \quad (5)$$

where x^*, u^* are the optimal augmented state and augmented controls from the iLQR execution, i indicates the i -th constraint functional, and ϕ is a hyperparameter. With this updated form of the cost functional there still exists a recurrence relation to calculate the optimal control updates, see [16].

III. QOC ON THE FLUXONIUM

In the following we study the quantum optimal control problem on the fluxonium qubit. The fluxonium qubit is a promising building block for superconducting circuits, and the experimental constraints we encode in the optimization reflect those of a realistic device. Furthermore, the accurate two-level approximation of the system Hamiltonian makes it efficient to perform quantum optimal control on a classical computer. In the two-level approximation the system Hamiltonian takes the form

$$H/h = f_q \frac{\sigma_z}{2} + a(t) \frac{\sigma_x}{2} \quad (6)$$

where $f_q = 14\text{MHz}$ is the qubit frequency at the flux frustration point, a is the flux drive amplitude, h is Planck's constant, and σ_x, σ_y are Pauli matrices. The flux amplitude a is experimentally realized by modulating the flux threading the device. We consider the task of constructing $Z/2$, $Y/2$, and $X/2$ gates for the fluxonium qubit subject to experimental constraints, decoherence, and systematic errors. We compare the gates we obtain with numerical methods to the analytically constructed gates reported in [12] for the same device.

In addition to imposing optimization constraints that reflect physical limitations of the apparatus, we impose constraints that improve the experimental realization of the control pulse. To ensure gates may be concatenated arbitrarily without inducing AWG ringing due to high-frequency transitions, we require $a(t=0) = a(t=t_N) = 0$. Furthermore, we require $\int_0^{t_N} a(t)dt = 0$. This constraint ensures the pulse has zero net flux, mitigating the hysteresis ubiquitous in flux bias lines. We require $-0.5\text{GHz} \leq a(t) \leq 0.5\text{GHz}$ to ensure the two-level approximation III remains valid. Additionally, we require that each gate achieves the desired state transition $|\psi_N\rangle = |\psi_f\rangle$. In addition to these constraints we penalize the norm of the first and second derivatives of the flux amplitude to ensure its smoothness, and in doing so mitigate AWG ringing. The optimization is performed over the second derivative of the flux amplitude $\frac{d^2}{dt^2}a$ which is contained in the augmented control vector. The first derivative $\frac{d}{dt}a$, proportional a , and integral $\int a$ flux amplitude terms are contained in the augmented state vector. They are obtained from the second derivative of the flux amplitude by integration in the dynamics function. Both the zero net flux and target quantum state constraint are then handled by ensuring the target augmented state is reached $x_N = x_f$. The equality and inequality constraints on a are handled with a bound constraint.

In addition to obeying experimental constraints and achieving low simulated gate errors, we desire to make our gates perform well in the presence of decoherence. Decoherence of the quantum state due to external noise is typically modeled by two phenomena: longitudinal relaxation and pure dephasing. They are modeled using their

$1/e$ decay times T_1 and T_ϕ respectively (see Appendix). The main contributions to longitudinal relaxation in our device are dielectric loss in the capacitor, resistive loss in the inductor, and Purcell loss. The main contributions to pure dephasing in our device are $1/f$ flux noise and decay via charge and flux coupling to the control lines. Dissipation to the thermal bath via longitudinal relaxation is an irreversible process that results in information loss. Conversely, pure dephasing is a reversible process. There is a tradeoff between the two decoherence processes. In the case of white noise the sum of the noise weights W_1 and W_ϕ is constant [3]. Our device achieves its best pure dephasing protection at the flux frustration point $T_{2e}(a=0) \sim 300\mu\text{s}$ where the qubit is first-order insensitive to changes in flux. It becomes more susceptible to pure dephasing as the flux is tuned away from the flux frustration point $|a| > 0$. Conversely, longitudinal relaxation is at a minimum at the flux frustration point $T_1(a=0) = 0.315\text{ms}$, and increases away from the flux frustration point $T_1(a=0.34\text{GHz}) = 4.3\text{ms}$. Given the nature of the decay processes and the tradeoff, we choose to maximize the longitudinal relaxation time directly by tuning the flux amplitude and employ robust control techniques to mitigate pure dephasing.

IV. LONGITUDINAL RELAXATION AWARENESS

The longitudinal relaxation time T_1 varies with control parameters in a range of superconducting circuit platforms. It is advantageous to tune the controls to extend the longitudinal relaxation time. Computing the gate error due to longitudinal relaxation requires propagating density matrices of size $n \times n$ under master equation dynamics, rather than state vectors of size n under the TDSE dynamics. We avoid this increase in computational complexity by penalizing the integrated rate of longitudinal relaxation, i.e. the probability of longitudinal relaxation. Using this probability as proxy for the gate error incurred is reasonable because losses due to longitudinal relaxation increase monotonically in time. This technique can be extended to error channels which share the monotonically increasing property. Additionally, for a constant T_1 time, a shorter gate duration would favor a lower longitudinal relaxation probability. We allow the optimizer to tune the gate duration in order to minimize the longitudinal relaxation probability. Our scheme for time-optimal control is applicable to any time-optimal problem, not only the one we study here.

The longitudinal relaxation probability is given by

$$P_1(t) = \int_0^t T_1^{-1}(a(t'))dt' \quad (7)$$

P_1 is penalized using a quadratic cost at each knot point $|P_1(t_k)|^2$. $T_1(a_k)$ is obtained at each knot point by evaluating a spline fit to experimental data of the form

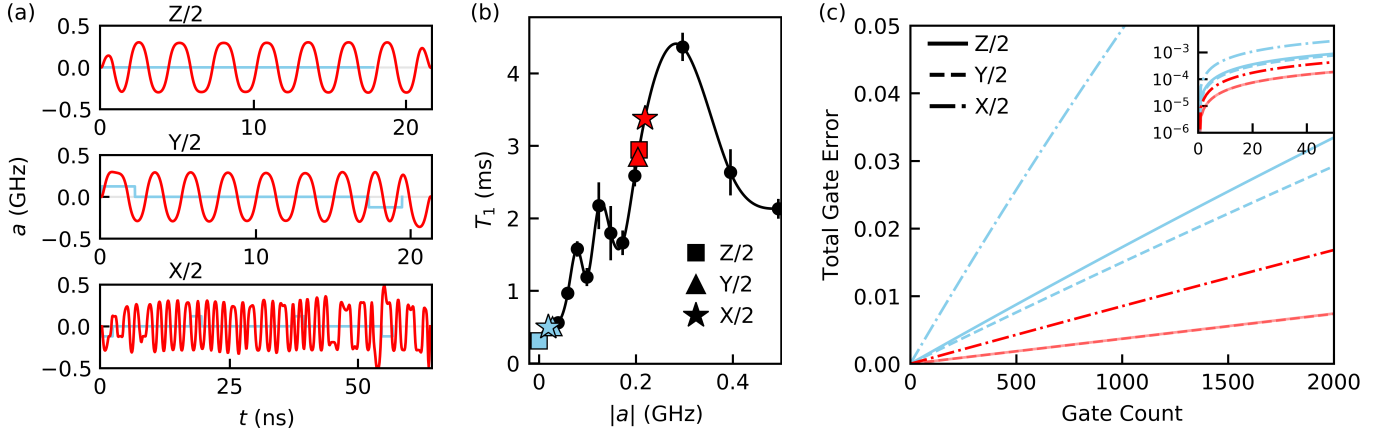


Figure 1: (a) Numerically optimized gates (red) and analytically optimized gates (blue). (b) T_1 interpolation function used in optimization. Markers denote the time-averaged, absolute amplitude of each gate. (c) Lindblad master equation simulation with T_1 dissipation for successive gate applications. The reported gate error is the cumulative gate error after each gate application. The numerically optimized $Z/2$ and $Y/2$ gate errors are indistinguishable in the figure.

$\{(a, T_1)\}$. It is also possible to use a spline fit to theoretically obtained data. However, T_1 values are known to fluctuate greatly with laboratory temperatures [24]. Interpolating T_1 from experimental data increases the fringe truth of the simulation.

We allow the optimizer to tune the gate duration by making the time step between each knot point Δt_k a decision variable. Promoting Δt_k to a decision variable, rather than the number of knot points N , preserves the Markovian decision structure of the trajectory optimization problem. To ensure numerical integration accuracy is maintained we add a bound constraint at each knot point $5e-2 \text{ ns} \leq \Delta t_k \leq 2e-1 \text{ ns}$. This bound constraint may be violated for intermediate iterations of the optimization, so we add the square root of the time step $\sqrt{\Delta t_k}$ to the augmented control vector and use the squared root of the time step $|\Delta t_k|$ in optimization.

We compare the numerical method we have developed to the analytic gates on the task of achieving low gate errors in the presence of longitudinal relaxation for the $Z/2$, $Y/2$, and $X/2$ gates. The numerically optimized gates converge on similar solutions, a periodic waveform with amplitude $\sim 0.2 \text{ GHz}$, see Figure 1. They extend their gate times beyond their analytic counterparts, trading longer gate times for access to higher amplitudes and therefore higher T_1 times. All numerical gates reduce their single gate errors by a factor of 5 over their analytic counterparts which is commensurate to their probability of longitudinal relaxation reductions, see Appendix. The gate error reported in this text is the infidelity of the evolved state and the target state averaged over 1000 pseudo-randomly generated initial states. The numerical $Z/2$ and $Y/2$ gates perform similarly in the concatenated gate application comparison, suppressing accumulated gate errors to $8 \cdot 10^{-3}$ over 2000 gate applications $\sim 40 \mu\text{s}$. The numerical $X/2$ gate achieves an accumu-

lated gate error of $1.7 \cdot 10^{-2}$ over 2000 gate applications $\sim 124 \mu\text{s}$. Both the analytic and numerical gates attain single gate errors sufficient for quantum error correction $< 10^{-4}$, requisite for fault-tolerant quantum computing. The low gate errors achieved by the numerical gates for extend computations are critical for noisy, intermediate-scale quantum (NISQ) applications. These improvements are significant for the realistic constraints we have imposed on the gates, and do not represent a fundamental limit to the optimization methods we have employed.

V. ROBUSTNESS TO STATIC PARAMETER DEVIATIONS

We have formulated the quantum optimal control problem as an open loop optimization problem, i.e. feedback from the experiment is not incorporated in optimization. However, the device typically deviates from the Hamiltonian we use in optimization, leading to poor experimental performance. To mitigate these errors we employ robust control techniques to make the state evolution insensitive to Hamiltonian parameter deviations. As an example we mitigate errors arising from the drift and finite measurement precision of the qubit frequency $\tilde{f}_q = f_q \pm \sigma_{f_q}$. We consider three robust control techniques. The first is the sampling method, which has been proposed previously in the context of QOC [8, 19, 20]. In the sampling method, multiple states are evolved under distinct deviant dynamics to capture the effect of parameter deviations. We also study the unscented sampling method which uses the unscented transformation to accurately propagate a distribution representing the uncertainty in an evolving state due to a parameter deviation. The unscented transformation was designed for nonlinear Kalman filtering and is frequently utilized in

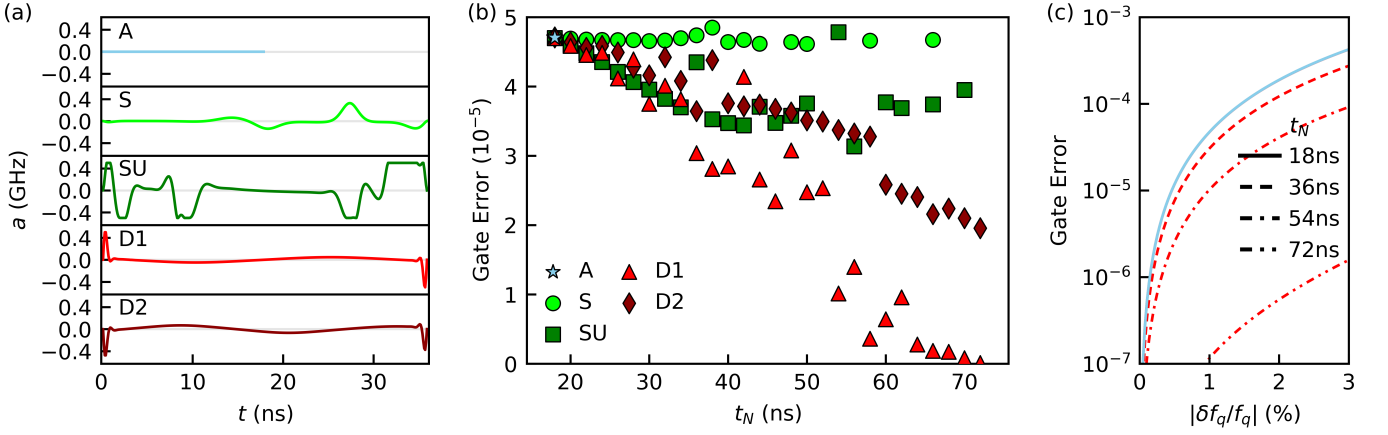


Figure 2: (a) $Z/2$ gates robust to qubit frequency detunings constructed with the analytic, sampling, unscented sampling, and the 1st- and 2nd-order derivative methods. The gates shown for the numerical methods are the solutions at twice the analytic gate time. (b) Single gate error as a function of the gate duration at a one-percent detuning from the nominal qubit frequency for all methods. Missing data points represent solutions with a gate error above $5 \cdot 10^{-5}$. (c) Single gate error as a function of the detuning from the nominal qubit frequency. The solutions for the analytic and 1st-order derivative methods are shown at multiples of the analytic gate time. The performance of the two methods is indistinguishable at the analytic gate time 18ns.

robust control [21–23]. Finally, we propose the derivative method. Derivative information encoding the sensitivity of the state trajectory with respect to the deviant parameter is used to penalize state trajectory deviations.

In the sampling method, sample states evolve under a Hamiltonian where a parameter is replaced by a deviant value. We propagate the additional states $|\psi^\pm\rangle$ with deviant values $\lambda^\pm = \lambda \pm \sigma_\lambda$. The gate error of each sample state is penalized at each knot point $1 - |\langle \psi_k^\pm | \psi_f \rangle|^2$. Each initial state is used to initialize two sample states $|\psi^\pm\rangle$. The initial states are chosen so that their outer products span the operators on the Hilbert space $\{|0\rangle, |1\rangle, (|0\rangle + i|1\rangle)/\sqrt{2}, (|0\rangle - i|1\rangle)/\sqrt{2}\}$ [25]. For this method the number of states in the augmented state vector scales as $O(dn^2)$ because each of n^2 initial states is represented by $2d$ samples. n is both the dimension of the Hilbert space and the size of the state vector. d is the number of deviant parameters.

The strategy of the unscented sampling method is to propagate an ensemble of sample states (sigma points) which represent a distribution over every element of the initial state. The distribution models the uncertainty in each state element arising from the parameter deviation. The ensemble consists of $2(n+d)$ states. Each state in the ensemble is propagated to the next knot point using separate deviant dynamics. Then, the mean and covariance of the propagated ensemble is calculated. New states are sampled from the distribution given by the calculated statistics for propagation to the next knot point. This resampling procedure, the unscented transformation, accurately propagates first and second moments of the distribution and ensures the points lie on the \sqrt{n} th covariance contour at each knot point. A detailed update procedure is given in the appendix. Each initial

state from the operator basis is represented with a distribution of $2(n+d)$ samples. Hence, the number of states in the augmented state vector scales as $O(n^3 + dn^2)$. The gate error of each sample state is penalized as in the sampling method.

The derivative method draws on the intuition that the sensitivity of the state evolution to a parameter λ is encoded in the l th-order derivative of the state with respect to that parameter $|\partial_\lambda^l \psi\rangle$. The m th-order derivative method minimizes the norm of the first m state derivatives with a quadratic cost at each knot point $|\langle \partial_\lambda^l \psi | \partial_\lambda^l \psi \rangle|^2$, $l \in \{1, \dots, m\}$. The state derivatives could be obtained with backwards mode differentiation. Naive automatic differentiation would compute the state derivative at all $1, \dots, k-1$ knot points to obtain the state derivative at knot point k . For a single state derivative and N knot points this requires $O(N^2)$ matrix multiplications. Instead, we forward propagate the state derivatives in the augmented state vector under coupled dynamics, resulting in $O(N)$ matrix multiplications. For example, the dynamics for the 1st-order derivative method are

$$i\hbar \frac{d}{dt} |\psi\rangle = H |\psi\rangle \quad (8)$$

$$i\hbar \frac{d}{dt} |\partial_\lambda \psi\rangle = H |\partial_\lambda \psi\rangle + (\partial_\lambda H) |\psi\rangle \quad (9)$$

Exponential integrators that account for the non-linear term may be used to efficiently integrate the coupled dynamics [26, 27]. For this method m state derivatives are associated with each initial state from the operator basis. So, the number of states in the augmented state vector scales as $O(dmn^2)$.

To demonstrate the applicability of these techniques to

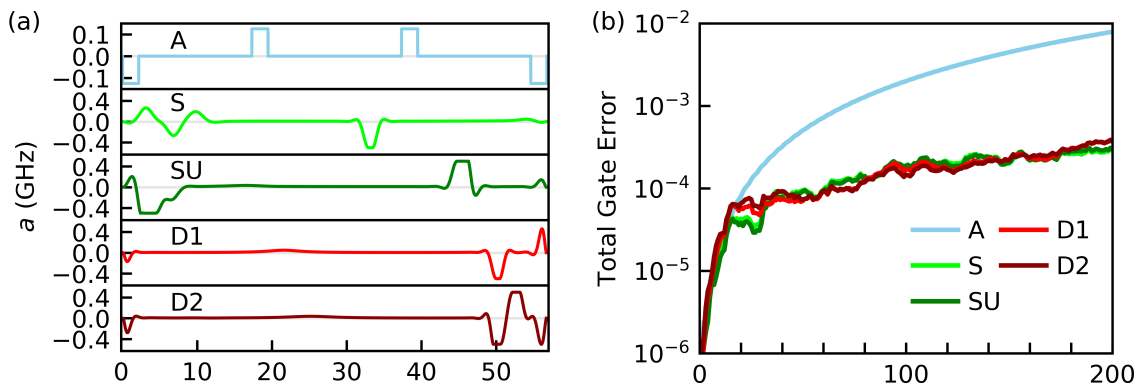


Figure 3: (a) $X/2$ gates robust to flux offsets constructed with the analytic, sampling, unscented sampling, and the 1st- and 2nd-order derivative methods. The gates shown are the solutions at the analytic gate time. (b) Simulation of stochastic $1/f$ flux noise for successive gate applications. The reported gate error is the cumulative gate error after each gate application.

mitigate system parameter deviations, we consider the task of achieving a single $Z/2$ gate subject to a constant qubit frequency detuning $f_q \leftarrow f_q + \delta f_q$. We take $\sigma_{f_q}/f_q = 1\%$ to be one standard deviation, and equip the sampling methods accordingly. For each method we compute the gate error for one simulated gate application subject to the deviant dynamics given by the stated qubit frequency detuning δf_q .

We compare the numerical methods to an analytically derived $Z/2$ gate. This gate corresponds to idling at the flux frustration point $a = 0$. The analytic gate is at the device's speed limit for a $Z/2$ gate $t_{Z/2} = 1/4f_q$ and is simple to derive. Its erroneous rotation angle $2\pi t_{Z/2}\delta f_q$ is linearly sensitive to the qubit frequency detuning, resulting in a gate error that is quadratically sensitive to the qubit frequency detuning. At a one-percent qubit frequency detuning the analytic gate achieves a gate error $\sim 4.5 \cdot 10^{-5}$, which is sufficient for quantum error correction, see Figure 2b. Although the analytic $Z/2$ gate performs well, it works only at the gate time $t_{Z/2}$. The ability to perform Z rotations in arbitrary times is critical for operating multi-qubit experiments in the lab frame. Each numerical method is able to find solutions at all gate times above $t_{Z/2}$, but is unable to find solutions at shorter times, see Figure 2b. These numerical methods offer an effective scheme for synchronizing qubits operating at different frequencies $f_{q,i} \neq f_{q,j}$.

The sampling and unscented sampling methods converge on qualitatively similar solutions which combine idling periods with fast ramps to the maximum amplitude. The gate error at a one-percent detuning from the nominal qubit frequency achieved by the sampling method does not improve substantially over the range of gate durations. The unscented sampling method achieves linear decreases in its gate error with longer gate durations until half the larmor period $1/2f_q$ after which it achieves a consistent gate error $\sim 3.5 \cdot 10^{-5}$. The derivative methods converge on qualitatively similar solutions that use fast traingle pulses at the boundaries and

balance time on either side of the flux-frustration point symmetrically at low amplitudes. Both methods achieve a super-linear scaling in their gate error as a function of the gate duration. The gate error for the 1st-order derivative method approaches zero at the larmor period $1/f_q$. We believe the 1st-order method outperforms the n^{d} -order method due to the low contribution of second-order terms to the gate error in this deviation regime, see Table 2.

Multiple analytic methods have also been presented to construct gates that mitigate the error arising from parameter deviations including composite pulse sequences [11], the DRAG scheme [28], and geometric phase considerations [6, 10]. Composite pulse sequences are derived by computing the erroneous rotation arising from the static parameter deviation with a finite order Magnus expansion. Pulses are then suitably composed to eliminate the error. In principle the error may be eliminated to arbitrary order with sufficiently many pulses. It is difficult to choose an appropriate composite pulse for comparison on the problem we study here. We propose comparing numerical methods to existing analytic techniques for future work.

VI. ROBUSTNESS TO STOCHASTIC PARAMETER DEVIATIONS

An additional source of experimental error arises from stochastic Hamiltonian parameter deviations. For many flux-biased and inductively-coupled superconducting circuit elements, magnetic flux noise is a significant source of coherent errors. Magnetic flux noise modifies the fluxonium qubit's amplitude from its nominal value by an amount δa . It is well studied that the spectral density of δa follows a $1/f$ distribution for a range of devices, consisting primarily of low frequency noise (citations needed). Analytic methods to combat $1/f$ noise take advantage of the low frequency characteristic and

treat the noise as quasi-static, performing generalizations of the spin-echo technique to compensate for erroneous drift. This is the strategy employed by the analytic gate considered here.

We compare the numerical methods discussed in the previous section on the task of realizing a $X/2$ gate subject to $1/f$ flux noise. The noise is generated by filtering white noise sampled from a standard normal distribution using a finite impulse response filter. It is then scaled by the flux noise amplitude of our device $A_\Phi = 5.21\mu\Phi_0 \implies \delta a \sim 2.5 \cdot 10^{-5}\text{GHz}$. The unscented sampling method is modified so that its sampled deviations follow a $1/f$ distribution by carrying the state of a finite impulse response filter in the augmented state vector. In principle the basic sampling method could be modified similarly but we choose to sample statically at δa for comparison. The derivative methods require no modification from the static case.

We simulate successive applications of the gate constructed by each method and compute the gate error after each application, see Figure 3. Both the analytic and numerical methods achieve single gate errors sufficient for quantum error correction. Despite converging on qualitatively different solutions, the numerical methods perform similarly in the concatenated gate application comparison, achieving a two order of magnitude reduction in gate error over the analytic gate at 200 gate applications $\sim 11\mu\text{s}$. Coherent errors are a significant source of error in NISQ applications and these numerical techniques give an effective method for mitigating them.

VII. CONCLUSION

In conclusion, we have demonstrated techniques for achieving robustness to systematic errors and mitigating decoherence on a quantum system using state-of-the-art trajectory optimization. We have proposed a scheme for mitigating longitudinal relaxation with time-optimal control and an efficient optimization metric that comes at a constant computational cost as opposed to integrating a master equation which scales quadratically with the dimension of the Hilbert space. We have proposed the derivative method for robust control which achieves super-linear gate error reductions in the gate duration for the problem we studied here. We have shown that robust control techniques can be used to mitigate decoherence due to $1/f$ flux noise, a dominant source of coherent errors for flux controlled qubits. The numerical techniques we have studied here can be used to perform phase gates in arbitrary times, which will be critical for synchronizing multi-qubit systems. Additionally, interleaving the error models with existing characterization methods will improve their effectiveness in experiments. These techniques will be employed to achieve the low gate errors required for fault-tolerant quantum computing applications.

ACKNOWLEDGMENTS

The authors would like to thank Helin Zhang for experimental assistance and Daniel Weiss for useful discussions.

Appendix A: Longitudinal Relaxation

The probability of longitudinal relaxation metric and gate error due to longitudinal relaxation metric are compared in Table I for the experiment shown in Figure 1c. The relative performance between the analytic and numerical techniques we study is similar across the two metrics.

| Gate | P_{1A}/P_{1N} | GE_A / GE_N |
|------|----------------------|---------------------|
| Z/2 | 5.745/1.149 = 5.000 | 1.776/0.371 = 4.787 |
| Y/2 | 5.253/1.157 = 4.540 | 1.539/0.370 = 4.159 |
| X/2 | 16.251/2.660 = 6.109 | 5.347/0.863 = 6.196 |

Table I: Single gate probability of longitudinal relaxation ratios and single gate error due to longitudinal relaxation ratios for the analytic and numerical methods. Both probabilities and gate errors are shown in units of 10^{-5} .

To compute the gate error due to longitudinal relaxation, we require the final state of the quantum system subject to longitudinal relaxation. To obtain the final state we employ the Lindblad master equation. This equation takes the form

$$\frac{d}{dt}\rho = \frac{-i}{\hbar}[H, \rho] + \sum_{i=1}^{n^2-1} \gamma_i (L_i \rho L_i^\dagger - \frac{1}{2}\{L_i^\dagger L_i, \rho\}) \quad (\text{A1})$$

Here $\rho = |\psi\rangle\langle\psi|$ is the density matrix, $n = \dim(\mathcal{H})$, and $[\cdot, \cdot], \{\cdot, \cdot\}$ are the algebraic commutator and anti-commutator. For longitudinal relaxation $\gamma_\uparrow = T_{1,\uparrow}^{-1}$, $\gamma_\downarrow = T_{1,\downarrow}^{-1}$, $L_\uparrow = \sigma^+/2$, and $L_\downarrow = \sigma^-/2$ where $\sigma^\pm = \sigma_x \pm i\sigma_y$. Both $T_{1,\uparrow}$ and $T_{1,\downarrow}$ are obtained from the spline shown in Figure 1b. The T_1 values in this spline are obtained experimentally by driving the qubit at the desired flux amplitude and monitoring the resultant decay. For more details consult [12].

Exponential integrators can be employed to integrate the Lindblad master equation using the Vectorization/Choi-Jamiolkowski isomorphism [29]

$$\frac{d}{dt}\text{vec}(\rho) = \hat{\mathcal{L}}\text{vec}(\rho) \quad (\text{A2})$$

$$\begin{aligned} \hat{\mathcal{L}} = & -i(I \otimes H - H^T \otimes I) \\ & + \sum_{i=1}^{n^2-1} \gamma_i (L_i^* \otimes L_i - \frac{1}{2}(I \otimes L_i^\dagger L_i - L_i^T L_i^* \otimes I)) \end{aligned} \quad (\text{A3})$$

Here $\rho = \sum_{i,j} \alpha_{i,j} |i\rangle \langle j|$ and $\text{vec}(\rho) = \sum_{i,j} \alpha_{i,j} |i\rangle \otimes |j\rangle$. We use zero-order hold on the controls so the integration is exact $\text{vec}(\rho_{k+1}) = \exp(\Delta t_k \hat{\mathcal{L}}_k) \text{vec}(\rho_k)$. This isomorphism transforms $(n^2 \times n^2) \times (n^2 \times n^2)$ matrix-matrix multiplications to $(n^4 \times n^4) \times n^4$ matrix-vector multiplications. For small n and zero-order held controls, we find that it is faster to use an exponential integrator on the vectorized equation than to perform Runge-Kutta on the unvectorized equation. The latter requires decreasing the integration time step to maintain accuracy, resulting in more knot points.

Appendix B: Unscented Transformation

In this section we outline the full unscented sampling procedure. First, we remark that ALTRO does not natively support complex numbers, so our optimization is performed under an isomorphism $\mathcal{H}(\mathbb{C}^n) \cong \mathcal{H}(\mathbb{R}^{2n})$.

$$H\psi \cong \begin{pmatrix} H_{\text{re}} & -H_{\text{im}} \\ H_{\text{im}} & H_{\text{re}} \end{pmatrix} \begin{pmatrix} \psi_{\text{re}} \\ \psi_{\text{im}} \end{pmatrix} \quad (\text{B1})$$

The unscented sampling method concerns a quantum state $\psi \in \mathbb{R}^{2n}$ with deviant parameters $\lambda \in \mathbb{R}^d$ and dynamics $\psi_{k+1} = f(\psi_k, \lambda_k)$. The nominal initial quantum state is given by ψ_0 with an associated positive-definite covariance matrix $P_0 \in \mathbb{R}_{++}^{n \times n}$ which describes the uncertainty in the initial state. P_0 is typically chosen to be non-zero even if the state preparation error is negligible. The deviant parameter is assumed to have zero mean and its distribution is given by the covariance matrix $L_k \in \mathbb{R}_{++}^{d \times d}$ at knot point k . The zero mean assumption is convenient for deriving the update procedure. A non-zero mean can be encoded in the dynamics f .

The initial $4n + 2d$ sigma points and initial $4n + 2d$ deviant parameters are sampled from the initial distributions

$$\begin{bmatrix} \Psi_0^i \\ \Lambda_0^i \end{bmatrix} = \begin{bmatrix} \bar{\Psi}_0 \\ 0 \end{bmatrix} \pm \beta \sqrt{\begin{bmatrix} P_0 & 0 \\ 0 & L_0 \end{bmatrix}}^i \quad (\text{B2})$$

We have written $\bar{\Psi}_0 = \psi_0$. β is a hyperparameter which controls the spacing of the covariance contour. The \pm is understood to take $+$ for $i \in \{1, \dots, 2n + d\}$ and $-$ for $i \in \{2n + d + 1, \dots, 4n + 2d\}$. We use the Cholesky factorization to compute the square root of the joint covariance matrix, though other methods such as the principal square root may be employed. The superscript indicates the i^{th} column of the lower triangular Cholesky factor. Then, the sigma points are normalized

$$\Psi_0^i \leftarrow \frac{\Psi_0^i}{\sqrt{\Psi_0^{iT} \Psi_0^i}} \quad (\text{B3})$$

The sigma points are propagated to the next knot point

$$\Psi_1 = f(\Psi_0, \Lambda_0) \quad (\text{B4})$$

The mean and covariance of the sigma points is computed

$$\bar{\Psi}_1 = \frac{1}{4n + 2d} \sum_{i=1}^{4n+2d} \Psi_1^i \quad (\text{B5})$$

$$P_1 = \frac{1}{\beta^2(4n + 2d)} \sum_{i=1}^{4n+2d} (\Psi_1^i - \bar{\Psi}_1)^T (\Psi_1^i - \bar{\Psi}_1) \quad (\text{B6})$$

The sigma points are then resampled and propagated to the next knot point using eq B2, B3, and B4.

Appendix C: Derivative Method

We believe the 1st-order derivative method tends to outperform the 2nd-order derivative method in the small, static detuning regime, see Figure 2b, because second-order contributions to the gate error are small. The norm of the state derivatives for the 1st- and 2nd-order derivative methods are provided in Table 2 for the solutions of the optimization outlined in section V at the gate duration $t_N = 38\text{ns}$.

| Method | $ \langle \partial_{f_q} \psi_N \partial_{f_q} \psi_N \rangle ^2 (10^3)$ | $ \langle \partial_{f_q}^2 \psi_N \partial_{f_q}^2 \psi_N \rangle ^2 (10^7)$ |
|--------|--|--|
| D-1 | 2.051 | 17.935 |
| D-2 | 2.511 | 7.628 |

Table II: Norm of the first basis state's derivate with respect to the qubit frequency for $Z/2$ gates optimized using the derivative methods. The norms are computed at the end of the gate's duration $t_N = 38\text{ns}$.

The dynamics for the derivative methods can be integrated efficiently using exponential integrators. General exponential integrators break the dynamics into a linear term and a non-linear term. For example, consider integrating the dynamics of the first state derivative $\frac{d}{dt} |\partial_\lambda \psi\rangle = H |\partial_\lambda \psi\rangle + (\partial_\lambda H) |\psi\rangle$ in units of $i\hbar = 1$. The linear term is $L = H$ and the non-linear term is $N = (\partial_\lambda H) |\psi\rangle$. With zero-order hold on the controls the exact propagation is

$$\begin{aligned} |\partial_\lambda \psi_{k+1}\rangle &= \exp(\Delta t_k L_k) |\partial_\lambda \psi_k\rangle \\ &+ \int_0^{\Delta t_k} \exp((\Delta t_k - t') L_k) N(t_k + t') dt' \end{aligned} \quad (\text{C1})$$

General exponential integrators proceed by breaking the integral into a discrete sum, similar to the procedure for Runge-Kutta schemes. We use a simple approximation known as the Lawson-Euler method [26]

$$\begin{aligned} |\partial_\lambda \psi_{k+1}\rangle &\approx \exp(\Delta t_k L_k) |\partial_\lambda \psi_k\rangle \\ &+ \exp(\Delta t_k L_k) N_k \end{aligned} \quad (\text{C2})$$

This method provides a good tradeoff between accuracy and efficiency, requiring one unique matrix exponential computation per stage. Exact integration accuracy is not of the utmost importance because the state derivatives

guide the robust optimization, and do not correspond to experimental parameters which must be realized with high accuracy.

-
- [1] N. Khaneja, T. Reiss, C. Kehlet, T. Schulte-Herbrüggen, and S. J. Glaser, Optimal control of coupled spin dynamics: design of nmr pulse sequences by gradient ascent algorithms, *Journal of magnetic resonance* **172**, 296 (2005).
 - [2] R. W. Heeres, P. Reinhold, N. Ofek, L. Frunzio, L. Jiang, M. H. Devoret, and R. J. Schoelkopf, Implementing a universal gate set on a logical qubit encoded in an oscillator, *Nature communications* **8**, 1 (2017).
 - [3] Z. Huang, P. S. Mundada, A. Gyenis, D. I. Schuster, A. A. Houck, and J. Koch, Engineering dynamical sweet spots to protect qubits from $1/f$ noise, *arXiv preprint arXiv:2004.12458* (2020).
 - [4] Z. Leng, P. Mundada, S. Ghadimi, and A. Houck, Robust and efficient algorithms for high-dimensional black-box quantum optimization, *arXiv preprint arXiv:1910.03591* (2019).
 - [5] N. Leung, M. Abdelhafez, J. Koch, and D. Schuster, Speedup for quantum optimal control from automatic differentiation based on graphics processing units, *Physical Review A* **95**, 042318 (2017).
 - [6] J. Xu, S. Li, T. Chen, and Z.-Y. Xue, Nonadiabatic geometric quantum computation with optimal control on superconducting circuits, *arXiv preprint arXiv:2004.10199* (2020).
 - [7] S. van Frank, M. Bonneau, J. Schmiedmayer, S. Hild, C. Gross, M. Cheneau, I. Bloch, T. Pichler, A. Negretti, T. Calarco, *et al.*, Optimal control of complex atomic quantum systems, *Scientific reports* **6**, 34187 (2016).
 - [8] P. Rembold, N. Oshnik, M. M. Müller, S. Montangero, T. Calarco, and E. Neu, Introduction to quantum optimal control for quantum sensing with nitrogen-vacancy centers in diamond, *arXiv preprint arXiv:2004.12119* (2020).
 - [9] J. Sørensen, M. Aranburu, T. Heinzel, and J. Sherson, Quantum optimal control in a chopped basis: Applications in control of bose-einstein condensates, *Physical Review A* **98**, 022119 (2018).
 - [10] Z. Han, Y. Dong, B. Liu, X. Yang, S. Song, L. Qiu, D. Li, J. Chu, W. Zheng, J. Xu, *et al.*, Experimental realization of universal time-optimal non-abelian geometric gates, *arXiv preprint arXiv:2004.10364* (2020).
 - [11] J. T. Merrill and K. R. Brown, Progress in compensating pulse sequences for quantum computation, *Quantum Information and Computation for Chemistry*, 241 (2014).
 - [12] H. Zhang, S. Chakram, T. Roy, N. Earnest, Y. Lu, Z. Huang, D. Weiss, J. Koch, and D. I. Schuster, Universal fast flux control of a coherent, low-frequency qubit, *arXiv preprint arXiv:2002.10653* (2020).
 - [13] P. S. Mundada, A. Gyenis, Z. Huang, J. Koch, and A. A. Houck, Floquet-engineered enhancement of coherence times in a driven fluxonium qubit, *arXiv preprint arXiv:2007.13756* (2020).
 - [14] M. Abdelhafez, D. I. Schuster, and J. Koch, Gradient-based optimal control of open quantum systems using quantum trajectories and automatic differentiation, *Physical Review A* **99**, 052327 (2019).
 - [15] N. Wittler, F. Roy, K. Pack, M. Werninghaus, A. S. Roy, D. J. Egger, S. Filipp, F. K. Wilhelm, and S. Machnes, An integrated tool-set for control, calibration and characterization of quantum devices applied to superconducting qubits (2020), *arXiv:2009.09866* [quant-ph].
 - [16] T. A. Howell, B. E. Jackson, and Z. Manchester, Altro: A fast solver for constrained trajectory optimization, in *2019 IEEE/RSJ International Conference on Intelligent Robots and Systems (IROS)* (IEEE, 2019) pp. 7674–7679.
 - [17] S. Machnes, E. Assémat, D. J. Tannor, and F. K. Wilhelm, Gradient optimization of analytic controls: the route to high accuracy quantum optimal control, *arXiv preprint arXiv:1507.04261* (2015).
 - [18] M. H. Goerz, D. Basilewitsch, F. Gago-Encinas, M. G. Krauss, K. P. Horn, D. M. Reich, and C. P. Koch, Krotov: A python implementation of krotov’s method for quantum optimal control, *SciPost physics* **7** (2019).
 - [19] A. R. Carvalho, H. Ball, M. J. Biercuk, M. R. Hush, and F. Thomsen, Error-robust quantum logic optimization using a cloud quantum computer interface, *arXiv preprint arXiv:2010.08057* (2020).
 - [20] P. Reinhold, *Controlling Error-Correctable Bosonic Qubits*, Ph.D. thesis, Yale University (2019).
 - [21] S. J. Julier and J. K. Uhlmann, Unscented filtering and nonlinear estimation, *Proceedings of the IEEE* **92**, 401 (2004).
 - [22] A. Lee, Y. Duan, S. Patil, J. Schulman, Z. McCarthy, J. Van Den Berg, K. Goldberg, and P. Abbeel, Sigma hulls for gaussian belief space planning for imprecise articulated robots amid obstacles, in *2013 IEEE/RSJ International Conference on Intelligent Robots and Systems* (IEEE, 2013) pp. 5660–5667.
 - [23] Z. Manchester and S. Kuindersma, Derivative-free trajectory optimization with unscented dynamic programming, in *2016 IEEE 55th Conference on Decision and Control (CDC)* (IEEE, 2016) pp. 3642–3647.
 - [24] P. Klimov, J. Kelly, Z. Chen, M. Neeley, A. Megrant, B. Burkett, R. Barends, K. Arya, B. Chiaro, Y. Chen, *et al.*, Fluctuations of energy-relaxation times in superconducting qubits, *Physical review letters* **121**, 090502 (2018).
 - [25] J. Chow, J. M. Gambetta, L. Tornberg, J. Koch, L. S. Bishop, A. A. Houck, B. Johnson, L. Frunzio, S. M. Girvin, and R. J. Schoelkopf, Randomized benchmarking and process tomography for gate errors in a solid-state qubit, *Physical review letters* **102**, 090502 (2009).
 - [26] H. Berland and B. Skaflestad, *Solving the nonlinear Schrödinger equation using exponential integrators*, Tech. Rep. (2005).
 - [27] L. Einkemmer, M. Tokman, and J. Loffeld, On the performance of exponential integrators for problems in magnetohydrodynamics, *Journal of Computational Physics* **330**, 550 (2017).
 - [28] P. Krantz, M. Kjaergaard, F. Yan, T. P. Orlando, S. Gus-

- tavsson, and W. D. Oliver, A quantum engineer's guide to superconducting qubits, *Applied Physics Reviews* **6**, 021318 (2019).
- [29] G. T. Landi, *Lecture notes on quantum information and quantum noise* (2018).